**Proceedings of the ASME 2023 Heat Transfer Summer Conference**
**SHTC2023**
**July 10–12, 2023, Washington DC, USA**

# SHTC2023-106993

# ESTIMATION OF HEAT FLUX FROM GASES RELEASED DURING THERMAL RUNAWAY OF LITHIUM-ION BATTERIES

**Ala' E. Qatramez[1], Andrew Kurzawski[2], John Hewson[2], Daniel Foti[1], Alexander J. Headley[1,*]**
[1]Department of Mechanical Engineering, University of Memphis, Memphis, Tennessee, 38152
[2]Fire Science and Technology Department, Sandia National Laboratories, Albuquerque, New Mexico, 87185

## ABSTRACT

*A jet is formed from venting gases of lithium-ion batteries (LIBs) during thermal runaway. Heat fluxes to surrounding surfaces from vented gases are calculated with simulations of an impinging jet in a narrow gap. Heat transfer correlations for the impinging jet are used as a point of reference. Three cases of different gap sizes ($H$) and jet velocities ($v_{Jet}$) are investigated and safety hazards are assessed. Local and global safety hazard issues are addressed based on average heat flux, average temperature, and average temperature rise in a cell. The Results show that about 40% to about 70% of venting gases energy can leave the module gap where it can be transferred to other modules or combust at the end of the gap if suitable conditions are satisfied. This work shows that multiple vents are needed to increase the temperatures of the other modules' cells to go into thermal runaway. This work is a preliminary assessment for future analysis that will consider heat transfer to the adjacent modules from multiple venting events.*

## 1 Introduction

Due to their special characteristics such as the high energy density and capacity [1, 2], lithium-ion batteries (LIBs) are the prime choice for different vital applications. Grid-scale energy storage systems (ESSs) are one such deployment where as of 2018 more than 90% of all ESSs in the United States utilize LIBs [2]. However, major incidents such as fires and explosions are hazards related to different LIB applications [3, 4]. Such events are associated with the failure of the batteries or during thermal runaway. Under extreme conditions, such as overheating, mechanical and electrical abuse, or due to manufacturing defects [5–7], LIBs undergo uncontrolled reactions leading to thermal runaway. In EESs, thermal runaway incidents have resulted in serious injuries [8, 9] and significant financial losses [10], where three possible mechanisms of explosion in LIB ESSs have been presented in [11].

During thermal runaway heat and gas are produced and released due to the reaction of the volatile and flammable electrolyte with the electrodes materials [12]. The venting rate of these gases changes with the cell materials and other parameters [13], as well as the cell temperature. Also, cell cathode chemistry effects on thermal runaway were investigated by Ref. [14]. More about basic LIB operating principles, cell reactions, components and design, thermal runaway mechanisms, and more can be found in Refs. [4, 15].

The estimated vent gas heat transfer-related characteristics identified in Ref. [16] are employed in this work to achieve the goal of this effort of estimating vent gas heat transfer in LIBs-ESSs. Qatramez *et al.* [16] used LIM1TR (Lithium-ion Modeling with 1-D Thermal Runaway), an open-source software model developed at Sandia National Laboratories, to estimate the vented gas characteristics such as venting time, Reynolds number, and composition by emulating LIB thermal propagation at the module level [17, 18] and experiments on 5 Ah pouch cells performed in Ref. [19], the dimensions of these cells are 75.5 mm $\times$64.5 mm $\times$9 mm [19]. Refs. [16, 19] showed that thermal runaway initiated by an external heat source takes longer time to start than a propagation-induced thermal runaway, while failure due to propagation has a longer venting time.

Though various experimental and numerical investigations [20–24] have undertaken the study of the conduction-dominated

*Email address for correspondence: jheadley@memphis.edu

thermal runaway propagation, the convection propagation via vent gas and its mechanics are less understood and merits further investigation. Vented gases exit the battery at relatively high temperatures and can transport heat from one part of an ESS to another where heating can lead to module-to-module thermal runaway propagation. Due to this, vented gases are a global hazard and can lead to serious safety issues in ESSs.

To achieve the goal of investigating convection propagation in ESSs computational fluid dynamics (CFD) simulations were used to calculate the heat transfer from the vented gasses as well as the impinging jet correlation. Four cases are studied to assess the safety hazards associated with venting gases in ESSs modules.

## 2 Methodology

### 2.1 Simulations

The simulations are based on the numerical solution to the fully compressible, multi-specie formulations of the Navier-Stokes, energy, and five species equations to account for the mass transport of $CO_2$, $H_2O$, $O_2$, and $C_2H_4$. These species are the vent gas components of the three reaction model used in LIM1TR. The scheme is based on a second-order accurate temporal and spatial discretization procedure [25]. The solution in time is integrated using an implicit dual-time formulation to eliminate approximate factorization errors [26] and allow for grids with high aspect ratios. The discretized inviscid and viscous operators are spatially integrated separately within a finite volume scheme. The inviscid fluxes are obtained from an upwind flux-vector splitting procedure using least-squared reconstruction of the primitive variables on the cell faces and Roe's approximate Riemann solver [27] to determine the fluxes on the faces. The divergence of the viscous fluxes is calculated using a Galerkin procedure. No reactions among the species are calculated, and no turbulence model is solved.

The equations are solved on a baseline two-dimensional unstructured grid of a domain of $1\,m \times 0.01\,m$ in the streamwise and transverse direction, respectively. The grid is meshed with $N = 112500$ grid cells with $Nx = 750$ grid cells and $Ny = 150$ grid cells in the streamwise and transverse direction, respectively, and is stretching in both directions. The grid is scaled in the vertical direction when the gap size $H$ is changed. Figure 1 shows the domain parameters namely; $H$, $L$ and $W$. A physical time step ($\Delta t$) of $1 \times 10^{-4}$s is employed, and the simulations are to reach steady state. The flow condition in the channel are given with a velocity $u = 0$ m/s , temperature $T_\infty = 300$ K, and pressure $P_\infty = 1$ atm before the jet enters the channel. Fixed wall temperatures for the cell, $T_w = 40\ ^o$ are imposed which is the operating temperature of the cell. The inflow boundary conditions are modeled by imposing a constant velocity $V_{Jet}$, $T_{Jet} = 800\ ^o$C which is in the range of vent gas temperature and $P_{in} = 1$ atm. The fluid is assumed to be calorically perfect solved with viscosity and thermal conductivity obtained at mean temperature $T_{mean} = (T_w + T_{Jet})/2$.

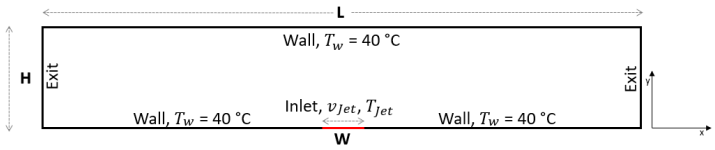


**FIGURE 1**. Venting gap and simulation domain, showing venting tear, gap height, gap length, and the boundary conditions. This figure is not to scale.

### 2.2 Heat Transfer Correlation

To achieve this goal an impinging jet correlation is used to calculate the heat transfer from the vented gasses. The results in Ref. [28] show that the effect of confinement on wall heat transfer coefficient is not significant for a jet-to-target distance greater than 0.5 ($H/D > 0.5$), also jet-to- target distance has less effect on stagnation region; since the significant effect was noticed for $H/D$ as low as 0.1. Behina *et al.* showed that stagnation correlations of unconfined impinging jet Nusselt number $Nu$ could be used for confined cases where $H/D > 0.5$, knowing that, in general, the average Nusselt number $\overline{Nu}$ decreases with confinement. The correlation of unconfined impinging jet Nusselt number will be applied for both regions: stagnation and wall jet. More interested readers are referred to [29, 30]. The impinging jet $\overline{Nu}$ for a single slot [31]

$$\frac{\overline{Nu}}{Pr^{0.4}} = \frac{3.06}{0.5/A_r + H/W + 2.78} Re_{Jet}^{m} \tag{1}$$

$$m = 0.695 - [\frac{1}{4A_r} + (\frac{H}{2W})^{1.33} + 3.06]^{-1}, \tag{2}$$

where $A_r$ and Re are defined as

$$A_r = \frac{W}{2x}, Re_{Jet} = \frac{V_{jet} 2W}{\nu},$$

and $D_h$= 2W is the hydraulic diameter. The validation conditions of this correlation are [31]

$$\begin{bmatrix} 300 \leq Re \leq 90000 \\ 2 \leq H/W \leq 10 \\ 0.025 \leq A_r \leq 0.125 \end{bmatrix}$$

Newton's cooling law can be used to calculate the average heat flux ($q^{''}$), $q^{''} = h(T_{Jet} - Ts)$, where $T_{Jet}$ and $T_s$ are the jet and surface temperatures, respectively. The convection heat transfer coefficient ($h$) can be calculated from $\overline{Nu} = \overline{h}D_h/k$ [31], where the $k$ is the thermal conductivity. Knowing that all the properties used for the correlation were for $CO_2$ at the mean temperature ($T_m = (T_{Jet} + T_s)/2$).

## 3 Results And Discussion

Four cases were studied in this work: case 1: $v_{Jet} = 58.5$ m/s and $H = 0.01$ m, case 2: $v_{Jet} = 58.5$ m/s and $H = 0.02$ m, case 3: $v_{Jet} = 7.0$ m/s and $H = 0.01$ m, and case 4: $v_{Jet} = 7.0$ m/s and $H = 0.02$ m. All cases have the same $W$ of 9 $mm$ which is the same as the cell thickness. In this section, time-averaged velocity ($\overline{u}$) and temperature ($\overline{T}$) profiles of each case are investigated to study the effects of $H$ and $v_{Jet}$ on the flow evolution especially the formation of channel flow. Heat fluxes are calculated for the four cases using simulations and correlations. After that, an analytical analysis for heat flux in the gap is derived to assess the hazards associated with these gases in EESs.

### 3.1 Mesh and Time Step Independence study

Before going through the simulation results, the sensitivity study of mesh and time step ($\Delta t$) is presented here before discussing the results. Figure 2 shows the time-averaged velocity ($\overline{u}$) and time-averaged temperature $\overline{T}$ profiles at five different locations based on for four cases derived from Case 1. Case 1b with the number of grid points in each direction half (Nx/2 $\times$ Ny/2) and nominal time step, case 1c where the grid is unchanged but an increased time step of $10\Delta t$ is used, and case 1d where the grid is unchanged but the time step is one-tenth the nominal time step. Figures 2(a)-(e) show that the $\overline{u}$ is relatively less sensitive to the decrease in the number of grid points. As the flow developed downstream, the profiles show signs of convergence. On the other hand, the larger time step shows large discrepancies between the nominal time step and the one-tenth time step case. Relatively, little differences exist between the small time step and the nominal time step cases. It should be noted that the one-tenth time step case is only averaged over a fraction of the time the nominal case is averaged. Figures 2(f)-(j) show similar convergence to the velocity. For the case of $\Delta t$ of $1^{-3}$, $\overline{T}$ profiles do match with other cases.

### 3.2 Flow Evolution

The effects of $H$ and $v_{Jet}$ are studied by looking at the $\overline{u}$ and $\overline{T}$ profiles at different locations along the simulated domain. Fig. 3 shows the $\overline{u}$ and $\overline{T}$ profiles at different $x = 0.6$, 0.7, 0.8, 0.9 and 1.0 m for the four cases, respectively.

Figure 3 shows that as flow goes through the channel both; $\overline{u}$ and $\overline{T}$ decrease. However, the temperature is still high enough

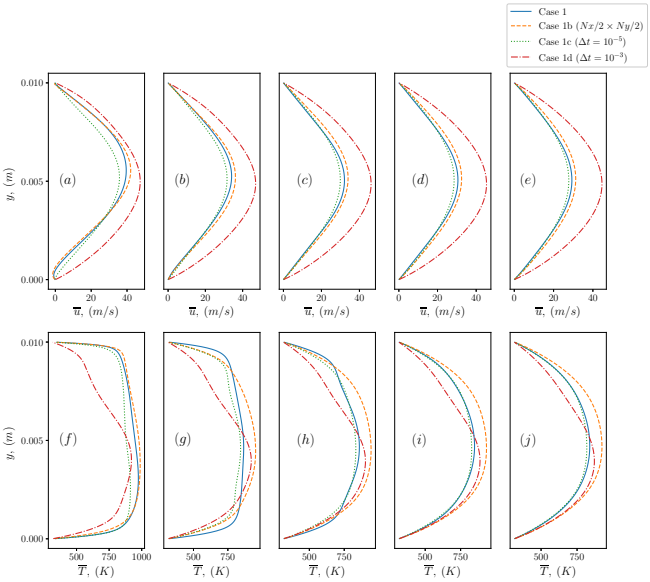


**FIGURE 2**. The time-averaged velocity ($\overline{u}$) and time-averaged temperature $\overline{T}$ profiles at (a) and (f) $x = 0.6$, (b) and (g) $x = 0.7$, (c) and (h) $x = 0.8$, (d) and (i) $x = 0.9$, and (c) and (j) $x = 1.0$ m for four cases: case 1, case 1(b), case 1(c), and case 1(d), respectively.

to cause serious thermal hazards to other cells and modules in the ESSs. For case 1, this temperature at the end of the gap ($x =$ 1 m) is about 800 K as shown in Fig. 3(a). Figure 3(a) and Figure 3(b) show that increasing $H$ has direct effect on $\overline{T}$ and $\overline{u}$ where they decrease as $H$ increases, since increasing $H$ increases the residence time for the flowing gases which slows the gases velocity and allow them to cool more. Figure 3(c) and Figure 3(d) show that as $v_{Jet}$ decreases $\overline{T}$ decreases significantly, where $v_{Jet}$ has more effect on $\overline{T}$ than $H$ for these ranges of $H$ and $v_{Jet}$ where slower $v_{Jet}$ results in much longer residence time for the gas to flow through the channel.

Such small gas sizes may not be enough to create a flammable mixture, but this high temperature can be enough to cause fire at the end of the channel where there is enough air to combust with the vent gas. As it shown in Fig. 3(a) and Fig. 3(d) and for same $H$, lower gap size is associated with high velocity at the end of the channel which enhanced the mixing with air there and increases the possibility of a wall fire over the module or rack casing.

The $\overline{u}$ and $\overline{T}$ profiles suggest that higher gap sizes are safer regarding the hazard of wall fire. However, a very high gap size may contain enough air to create a combustible mixture in the venting gap. These profiles also suggest smaller batteries with sizes to be stored in modules; since batteries with small sizes vent less amount of gas which is directly related to $v_{Jet}$.

The jet is nearly hydraulically fully developed for all cases

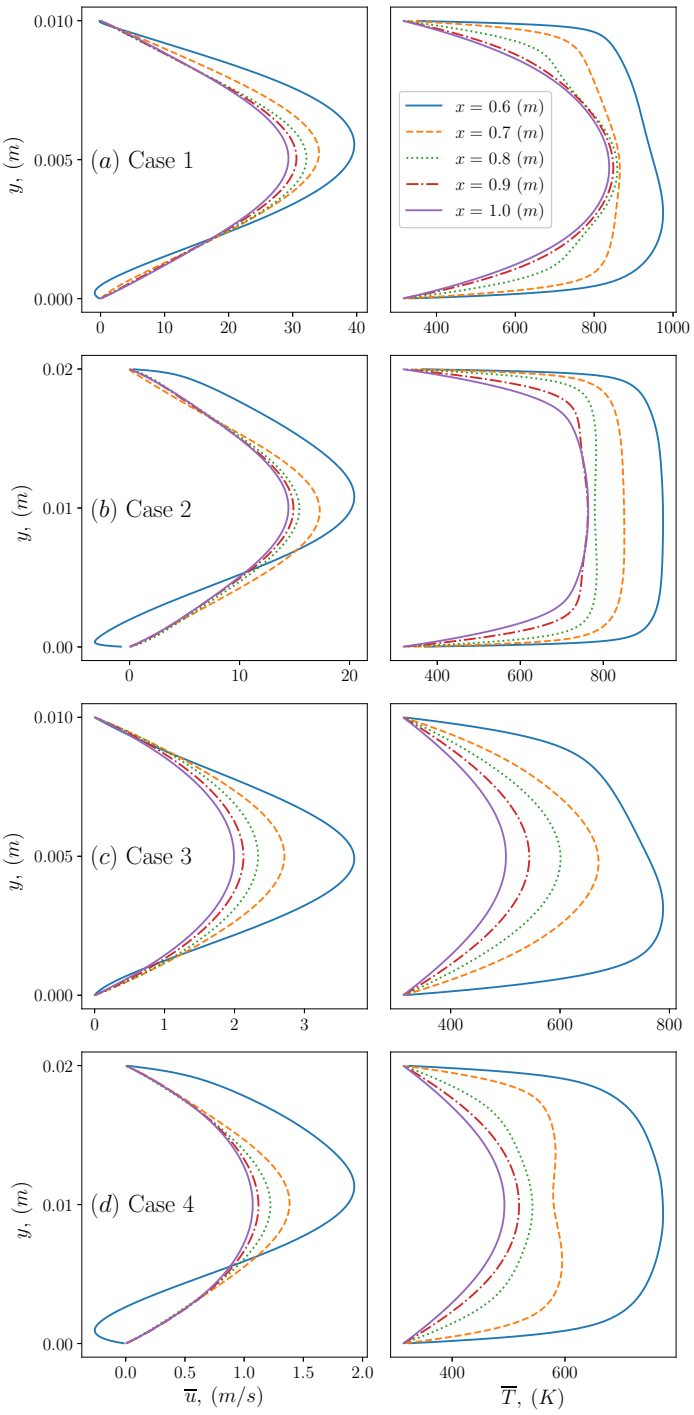


**FIGURE 3**. The time-averaged velocity ($\overline{u}$) and time-averaged temperature $\overline{T}$ profiles at $x = 0.6$, 0.7, 0.8, 0.9 and 1.0 m at $t = 2.5$ s for (a) case 1, (b) case 2, (c) case 3, and (d) case 4, respectively.

as the $\overline{u}$ profiles show in Fig. 3. The jet in case 2, case 3 and case 4 have not yet converted to thermally fully developed flow as it is shown in Fig. 3(b)-(d), while case 1 is nearly thermally fully developed at about $x = 0.9$ m.

Figure 4 shows the contours of $\overline{u}$ and $\overline{T}$ for $v_{Jet} = 58.5$ m/s and $H = 0.01$ m simulation. The contours in Fig. 4 agree with the $\overline{u}$ and $\overline{T}$ of Fig. 3(a) where the flow is approaching being fully developed at distance between $x = 0.8$ m and $x = 0.9$ m. It is important to mention that the contours show the need for a turbulence model to account for the mixing in the region between the impingement point and about 0.1 m from it. Also, when averaged over about 2 s of simulation time, the $\overline{T}$ profile at the wall is about 0.6% higher on the right side of the domain than the left.

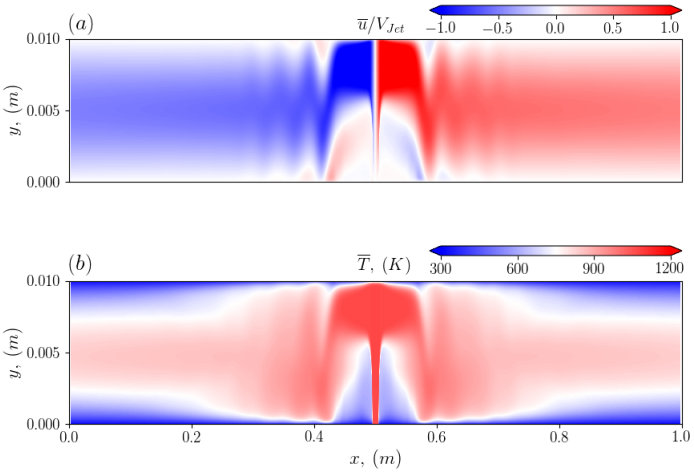


**FIGURE 4**. The contours of (a) average velocity ($\overline{u}$) and (b) average temperature ($\overline{T}$), respectively for case 1 ($v_{Jet} = 58.5$ m/s and $H = 0.01$ m) at $t = 2.5$ s. Note that the scale aspect ratio ($L/H = 100$).

### 3.3 Heat Flux Estimation

The heat fluxes were calculated at the top wall from the gas jet. For simulations, $q''$ were calculated from $-k(dT/dy)$ where k is the mixture thermal conductivity at the wall temperature. local Nusselt number ($Nu$) was determine as $(-dT/dy)/((T_{Jet} - T_s)/W)$ in Ref. [32]. In our case, $-dT/dy$ and $\overline{Nu}$ were computed from $\overline{T}$, the time-averaged velocity, values of the simulations. The impinging jet correlation and Newton's cooling law were used as a point of reference of the simulations results to calculate $\overline{Nu}$ and $q''$. $q''$ and $\overline{Nu}$ values along the right side of the gap are shown in Fig. 5.

The correlation results were discussed and compared in the valid region between the vertical lines shown in Fig. 5. It is important to mention that for case 1 and case 3, the gap size to jet width ($H/W = 1.1$) is below the lower limit of the correlation

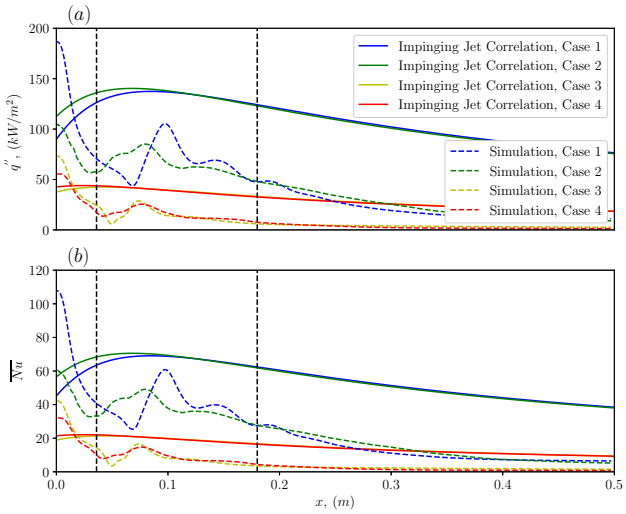


**FIGURE 5**. (a) Average heat flux ($q''$) at the top wall for all case calculated from the simulations and impinging jet correlation, (b) Average Nusselt number ($\overline{Nu}$). The vertical dashed lines are the valid $x$ limits for the correlation.

conditions, but they were chosen to match as close as possible the gap size of the battery modules.

From Fig. 5 and in the valid $x$ region, we see clearly that the correlation estimates higher $q''$ and $\overline{Nu}$ than the simulations for each corresponding case, so they many be used for safety design in that region. However, they are not recommended at the impinging point above the jet exit. The correlation and Simulations, as it is expected, show that low $v_{Jet}$ is associated with lower heat fluxes.

In the correlation valid region and for the correlation and simulation, the $H$ effect on $q''$ and $\overline{Nu}$ is not as clear as the $v_{Jet}$ effect where $H = 0.02$ cm cases result in higher heat fluxes at the beginning then decreases to be about equal to the lower $H$ as it is shown from the correlation, where from the simulations there are fluctuations as shown in Fig. 5. However, lower $H$ cases are associated with higher heat flux peaks at that region. We note that below the $H/W$ limit, there is little change in the Nusselt number within the valid $x$ limits, whereas within the valid $H/W$ limits the correlation is more sensitive to $H$.

For the simulations, the results show that for the small gap size more heat transferred to other modules from the wall, this high heat flux can be due to the poor mixing between the fluid parts in this small gap so more heat is concentrated at impinging point. Fig. 5 also shows another peak within about 10 cm from the impinging point. For safety design purposes, relatively high gaps are suggested up to a limit that does not satisfy the lower flammability limit. $\overline{T}$ and $\overline{u}$ profiles in Fig. 3 as well as heat flux values from Fig. 5 show that low $H$ and high $v_{Jet}$ are associated with more safety issues in terms of creating the atmosphere of wall file at the end of the space due to higher temperature and velocity, as well as the possible heat transfer to an upper module at the venting location and with small distance from it.

From simulation and after about 20 to about 40 cm from the impinging point, case 2 (the high $H$ case) shows higher heat fluxes than case 1 (the low $H$ case). After that cases with low $H$ shows slightly higher heat flux values. It is worth mentioning that it is important to use a turbulent model to emulate the mixing effect in the region within about 20 cm from the impinging point which will be the focus of future work. Also, these heat fluxes estimated by the simulations and from correlation are the highest possible fluxes that can be transferred from these gasses since a constant $T_W$ is used as a boundary condition in the simulations, and constant $T_W$ and $T_{Jet}$ are used in Newton's cooling low with the correlation to estimate these heat fluxes. This is sometimes referred to as the "cold wall" heat flux.

### 3.4 Heat Transfer Analysis And Hazard Assessment in The Venting Gap

In this part, we are conducting an analysis of the energy flows for all cases based on the average temperature of the flow and the heat flux to the top and bottom surfaces. Tracking the energy of the flow helps in evaluating the possible hazards associated with the outflow gasses that may leave the module and move to other parts.

For steady flow conditions, the mass flux per length of the jet $m'$ into the two-dimensional channel gap is $V_{Jet}\rho W$. Away from jet exit, the flow goes in two opposite directions down along the channel, so $m'$ in each direction is $m'/2$.

The thermal energy flow per unit length ($m'h_{T(x)}/2$) from the flowing gases in one direction of a 2-D channel can be found by integrating the average temperature $\overline{T}$ across the gap height

$$\frac{m'h_{T(x)}}{2} = \int_{y=0}^{y=H} \overline{\rho}\overline{c}_p\overline{u}(y,x)\overline{T}(y,x)dy \tag{3}$$

where $h_{T(x)}$ is the specific enthalpy of the gas, and $\overline{u}(y,x)$ and $\overline{T}(y,x)$ are the time-averaged axial velocities and temperatures at certain $x$ location. $\overline{c}_p$ is the gas mixture specific heat at $T_{mean}$, $\overline{\rho}$ is the mixture density calculated at average temperature $\overline{T}$ and average pressure $\overline{P}$ at certain $x$ location.

$q'_{Top}$ and $q'_{Bottom}$ are the cumulative heat transferred per unit length calculated at the top and bottom surfaces, respectively as:

$$\begin{aligned} q'_{Top} &= \int_{x=0.5}^{x=x} q''_{Top}\,dx \\ q'_{Bottom} &= \int_{x=0.5+W}^{x=x} q''_{Bottom}\,dx \end{aligned} \tag{4}$$

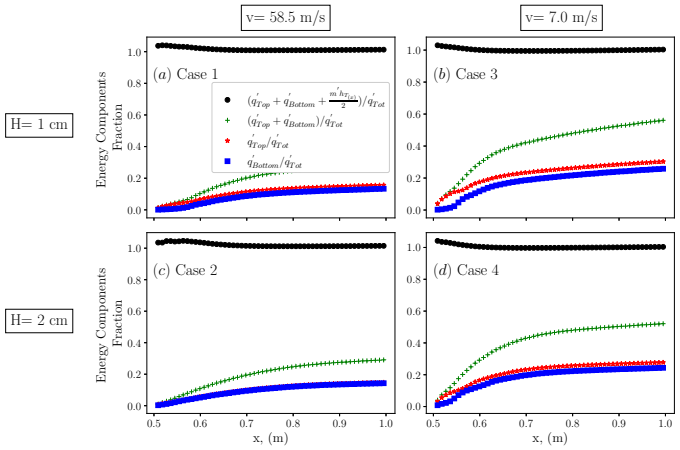


**FIGURE 6**. The sum of $q^{'}_{Top} + q^{'}_{Bottom} + \frac{m^{'} h_{T(x)}}{2}$ over the total vented energy per length $= 0.5\, W\, V_{Jet}\, \rho_{Jet}\, \overline{c}_p\, T_{Jet}$ that vented gases contain for: (a) case 1: $V = 58.5$ m/s, $H = 1$ cm, (b) case 3: $V = 7.0$ m/s, $H = 1$ cm, (c) case 2: $V = 58.5$ m/s, $H = 2$ cm, (d) case 4: $V = 7.0$ m/s, $H = 2$ cm.

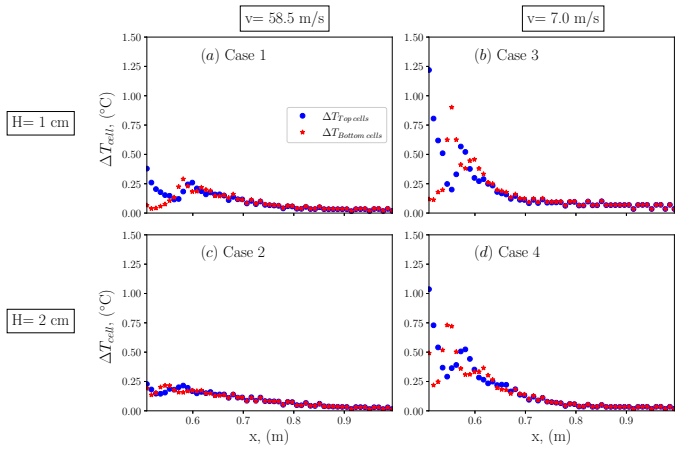


**FIGURE 7**. The average temperature rise of the cells in contact with the top and the bottom walls ($\Delta T_{cell}$) along the channel for: (a) case 1: $V = 58.5$ m/s, $H = 1$ cm, (b) case 3: $V = 7.0$ m/s, $H = 1$ cm, (c) case 2: $V = 58.5$ m/s, $H = 2$ cm, (d) case 4: $V = 7.0$ m/s, $H = 2$ cm.

The sum of these quantities defined in Eq. 3 and Eq. 4 should equal half of the total vented energy per length $q^{'}_{Tot} = 0.5\, W\, V_{Jet}\, \rho_{Jet}\, \overline{c}_p\, T_{Jet}$ that vented gases contain. These quantities in Eqs. 3 and Eqs. 4 are shown in Fig. 6 normalized by $q^{'}_{Tot}$ for the four cases along the right half of the channel from $x = 0.5$ m to 1.0 m by $W$ increments, where $\rho_{Jet}$ is the density at jet exit conditions. Case 1 compared with 3, and case 2 compared with 4 show the effect of $V_{Jet}$ on the heat transfer in the channel. The total loss to both surfaces with respect to the total vent gasses energy increases as the velocity decreases, where about 60% of the total heat is transferred to the upper and lower modules before the gasses leave the module assuming no heat transfers to the adjacent cells and that all gasses do leave the module at the gap end. Comparing the cases, increasing $v_{vent}$ and $H$ decreases the difference between $q^{'}_{Top}/q^{'}_{Tot}$ and $q^{'}_{Bottom}/q^{'}_{Tot}$. This figure shows that there is a significant amount of energy (about 40% to about 70%) leaves the gap/module, this energy can be transferred to other parts of an ESS or can cause a wall fire at the exit if other conditions are satisfied such as lower flammability limit. Finally, a little increase above 1 at the impingement point are shown in the figure which can be due to the high temperature gradients at that region as well as using constant k for the mixture for post-processing the heat fluxes.

To complete the picture, Figure 7 shows the average temperature rise of each 9 mm cell in contact with the top and the bottom walls resulting from the heat fluxes on the walls that is indicative of the amount of energy deposited into that cell ($\Delta T_{cell}$) for the four cases. Each point of $x$ in Fig. 7 represents the each cell center location. $\Delta T_{cell}$ is calculated as

$$\Delta T_{cell} = \frac{q^{'}_{cell}\, t_{vent}\, L_{cell}}{m_{cell}\, cp_{cell}} \tag{5}$$

where $q^{'}_{cell}$ is the energy deposited over the cell width, the $t_{vent}$ is the venting time associated to each $v_{vent}$, $L_{cell}$ is the length of the cell surface for the 5 Ah cell perpendicular to the 2-D simulation domain which is 75.5 mm, where the cell dimensions are 75.5 mm $\times$64.5 mm $\times$9 mm [19], $m_{cell}$ is the 5 Ah cell mass of 90.2 g [19], and $cp_{cell}$ is the estimated specific heat of the cell used in the simulations of 778.0 J/kg/K. $t_{vent}$ is calculated from the mass conservation of the vent gas for each $v_{vent}$ as $t_{vent} = Volume_{gas}/(v_{vent} * (A_{cell})$, where $Volume_{gas}$ is the total vent gas volume of about 10 liters, and $A_{cell}$ is the cell area perpendicular to the 2-D simulation domain. This concession must be made for mass and energy conservation when extrapolating from the 2-D approximation to the 3-D cell geometry.

Calculating $\Delta T_{cell}$ helps in identifying the possibility of these cells going into thermal runaway since thermal runaway occurs at certain temperature around 150 °C to 200 °C. In general, Figure 7 shows an increase of temperatures that do not lead to a critical temperature where thermal runaway starts. However, these $\Delta T_{cell}$ values are calculated for short venting times and one cell venting, so these $\Delta T_{cell}$ values can be significant for longer venting times and more than one failing cell. So, these values of $\Delta T_{cell}$ are indicative of the total energy deposited into adjacent cells from the venting of a single cell at a given $x$ distance away. It is also important to mention that the $\Delta T_{cell}$ are calculated assuming a uniform distribution of the heat from the vent gas along

the cell contact area. However, the localized heat from a venting jet can lead to more significant cell temperature rise. This is a first step for future analysis that will consider heat transfer to the adjacent modules from multiple venting events, since the analysis shows that one cell is not enough to cause propagation to another module. Ultimately, it takes multiple cells failing sequentially, and this analysis is the stepping stone to solving that problem.

For the four cases in Fig. 7, the cells near the impingement point experience higher $\Delta T_{cell}$, especially the cell just above the jet exit. As shown in this figure the cases of lower $V_{vent}$ are associated with higher $\Delta T_{cell}$, and that is because of their higher $t_{vent}$ (see Eq. 5). Generally, the lower $H$ cases show slightly higher $\Delta T_{cell}$ values. In general and for all cases, $\Delta T_{cell}$ for both top and bottom cells become almost equal at about 20 cm from the impingement point where $\Delta T_{cell}$ values are low.

This effort shows that the total heat transfer is more sensitive to the venting velocity. From observations, cell venting times are typically in the order of 5 to 20 s depending on the cause of the failure, and this duration in combination with the tear size can have a large influence on velocity. However, the tear size and its location are sources of uncertainty. The two different venting velocities included here can be associated with two different tear sizes.

In summary, local and global effects are associated with vent gas heat transfer. Such hazards can compromise the safety of an ESS which can lead to partial or full damage of a rack in thermal runaway, so serious efforts should be taken to focus on vent gas hazards, especially convective thermal runaway propagation along with conduction thermal runaway propagation.

## 4 Conclusions

The safety of ESSs is compromised by LIBs vent gas. These gasses form impinging jet during thermal runaway where heat can be transferred to other parts of an ESS by the vent gas. This study shows about 30% to 60% of the vented thermal energy is transferred to modules adjacent to gaps; the remaining thermal energy can leave the module gap where possible wall fires can occur along the ESS rack wall. Heat transfer at the wall of the module casing was calculated from CFD simulations and impinging jet correlation for four different cases. Results suggest designing the modules with a relatively high gap reduces the direct heat transferred to the upper module. This work shows that multiple and sequential failures of cells are needed to increase the temperatures of the cells in other modules to go into thermal runaway. For future work, a turbulence model will be added to investigate the effect of mixing in the impinging region, also the effect of other gap and slot sizes will be studied.


## Acknowledgements

This article has been authored by an employee of National Technology Engineering Solutions of Sandia, LLC under Contract No. DE-NA0003525 with the U.S. Department of Energy (DOE). The employee owns all right, title and interest in and to the article and is solely responsible for its contents. The United States Government retains and the publisher, by accepting the article for publication, acknowledges that the United States Government retains a non-exclusive, paid-up, irrevocable, worldwide license to publish or reproduce the published form of this article or allow others to do so, for United States Government purposes. The DOE will provide public access to these results of federally sponsored research in accordance with the DOE Public Access Plan https://www.energy.gov/downloads/doe-public-access-plan. This paper describes objective technical results and analysis. Any subjective views or opinions that might be expressed in the paper do not necessarily represent the views of the U.S. Department of Energy or the United States Government.


## REFERENCES


[1] Kim, D. K., Yoneoka, S., Banatwala, A. Z., Kim, Y.-T., and Nam, K., 2018. "Handbook on battery energy storage system". *Asian Development Bank: Manila, Philippines*. URL https://www.adb.org/publications/battery-energy-storage-system-handbook.

[2] EIA, U., 2020. "Battery storage in the united states: an update on market trends". *US Energy Information Administration (EIA)*.

[3] Battery modules "overheat" at vistra's moss landing energy storage facility. URL https://kion546.com/news/local-news/top-stories/2021/09/06/battery-modules-overheat-at-vistras-moss-landing-energy-storage-facility/.

[4] Wang, Q., Ping, P., Zhao, X., Chu, G., Sun, J., and Chen, C., 2012. "Thermal runaway caused fire and explosion of lithium ion battery". *Journal of power sources,* ***208***, pp. 210–224.

[5] Diaz, L. B., He, X., Hu, Z., Restuccia, F., Marinescu, M., Barreras, J. V., Patel, Y., Offer, G., and Rein, G., 2020. "Meta-review of fire safety of lithium-ion batteries: Industry challenges and research contributions". *Journal of The Electrochemical Society,* ***167***(9), p. 090559.

[6] Ouyang, D., Chen, M., Huang, Q., Weng, J., Wang, Z., and Wang, J., 2019. "A review on the thermal hazards of the lithium-ion battery and the corresponding countermeasures". *Applied Sciences,* ***9***(12), p. 2483.

[7] Feng, X., Ouyang, M., Liu, X., Lu, L., Xia, Y., and He, X., 2018. "Thermal runaway mechanism of lithium ion battery for electric vehicles: A review". *Energy Storage Materials,* ***10***, pp. 246–267.

[8] Dispute erupts over what sparked an explosive li-ion energy storage accident. URL https://spectrum.ieee.org/dispute-erupts-over-what-sparked-an-explosive-liion-energy-storage-accident.

[9] Hill, D., 2020. *McMicken Battery Energy Storage System Event: Technical Analysis and Recommendations*. DNV GL Energy Insights USA, Incorporated.

[10] Fires raise concern over energy storage battery safety in south korea. URL https://www.infolink-group.com/en/storage/energy-storage-market-trends/fires-raise-concern-over-energy-storage-battery-safety-in-south-korea.

[11] Zalosh, R., Gandhi, P., and Barowy, A., 2021. "Lithium-ion energy storage battery explosion incidents". *Journal of Loss Prevention in the Process Industries,* ***72***, p. 104560.

[12] Roth, E. P., and Orendorff, C. J., 2012. "How electrolytes influence battery safety". *The Electrochemical Society Interface,* ***21***(2), p. 45.

[13] Blum, A. F., and Long Jr, R. T., 2016. *Fire Hazard Assessment of Lithium Ion Battery Energy Storage Systems*. SpringerBriefs in Fire. Springer, New York.

[14] Golubkov, A. W., Fuchs, D., Wagner, J., Wiltsche, H., Stangl, C., Fauler, G., Voitic, G., Thaler, A., and Hacker, V., 2014. "Thermal-runaway experiments on consumer li-ion batteries with metal-oxide and olivin-type cathodes". *Rsc Advances,* ***4***(7), pp. 3633–3642.

[15] Preger, Y., Torres-Castro, L., and McDowall, J., 2020. *CHAPTER 3: LITHIUM-ION BATTERIES. The 2020 U.S. Department of Energy (DOE) Energy Storage Handbook (ESHB)*. Sandia National Laboratories Albuquerque, NM, USA.

[16] Qatramez, A., Kurzawski, A., Hewson, J., Parker, M., Porter, A., Foti, D., and Headley, A. J., 2022. "Characterization of vented gas predictions in lithium-ion modeling with 1-d thermal runaway (lim1tr)". In Heat Transfer Summer Conference, Vol. 85796, American Society of Mechanical Engineers, p. V001T06A001.

[17] Kurzawski, A., and Shurtz, R., 2019. LIM1TR: Lithium-ion Modeling with 1-D Thermal Runaway v1.0. Tech. Rep. SAND2021-12281, Sandia National Lab, (SNL-NM), Albuquerque, NM (United States).

[18] Kurzawski, A. Lim1tr: Lithium-ion modeling with 1-d thermal runaway. ULR https://github.com/ajkur/lim1tr.

[19] Archibald, E., Kennedy, R., Marr, K., Jeevarajan, J., and Ezekoye, O., 2020. "Characterization of thermally induced runaway in pouch cells for propagation". *Fire technology,* ***56***(6), pp. 2467–2490.

[20] Lamb, J., Orendorff, C. J., Steele, L. A. M., and Spangler, S. W., 2015. "Failure propagation in multi-cell lithium ion batteries". *Journal of Power Sources,* ***283***, pp. 517–523.

[21] Torres-Castro, L., Kurzawski, A., Hewson, J., and Lamb, J., 2020. "Passive mitigation of cascading propagation in multi-cell lithium ion batteries". *Journal of The Electrochemical Society,* ***167***(9), p. 090515.

[22] Li, Q., Yang, C., Santhanagopalan, S., Smith, K., Lamb, J., Steele, L. A., and Torres-Castro, L., 2019. "Numerical investigation of thermal runaway mitigation through a passive thermal management system". *Journal of Power Sources,* ***429***, pp. 80–88.

[23] Feng, X., He, X., Ouyang, M., Lu, L., Wu, P., Kulp, C., and Prasser, S., 2015. "Thermal runaway propagation model for designing a safer battery pack with 25 ah linixcoymnzo2 large format lithium ion battery". *Applied energy,* ***154***, pp. 74–91.

[24] Feng, X., Lu, L., Ouyang, M., Li, J., and He, X., 2016. "A 3d thermal runaway propagation model for a large format lithium ion battery module". *Energy,* ***115***, pp. 194–208.

[25] Lian, C., Xia, G., and Merkle, C. L., 2009. "Solution-limited time stepping to enhance reliability in cfd applications". *Journal of Computational Physics,* ***228***(13), pp. 4836–4857.

[26] Harvazinski, M. E., Huang, C., Sankaran, V., Feldman, T. W., Anderson, W. E., Merkle, C. L., and Talley, D. G., 2015. "Coupling between hydrodynamics, acoustics, and heat release in a self-excited unstable combustor". *Physics of Fluids,* ***27***(4), p. 045102.

[27] Roe, P. L., 1981. "Approximate riemann solvers, parameter vectors, and difference schemes". *Journal of computational physics,* ***43***(2), pp. 357–372.

[28] Behnia, M., Parneix, S., and Durbin, P., 1997. "Accurate modeling of impinging jet heat transfer". *Center for Turbulence Research, Annual Research Briefs*, pp. 149–164.

[29] Zuckerman, N., and Lior, N., 2006. "Jet impingement heat transfer: physics, correlations, and numerical modeling". *Advances in heat transfer,* ***39***, pp. 565–631.

[30] Martin, H., 1977. "Heat and mass transfer between impinging gas jets and solid surfaces". In *Advances in heat transfer*, Vol. 13. Elsevier, pp. 1–60.

[31] Incropera, Frank P., D. D. P. B. T. L. L. A. S., 2012. *Principles of Heat and Mass Transfer*. John Wiley Sons.

[32] Jaramillo, J., Trias, F., Gorobets, A., Pérez-Segarra, C., and Oliva, A., 2012. "Dns and rans modelling of a turbulent plane impinging jet". *International Journal of Heat and Mass Transfer,* ***55***(4), pp. 789–801.